

# Mapping the positions of Two-Level-Systems on the surface of a superconducting transmon qubit

Jürgen Lisenfeld,<sup>1,\*</sup> Alexander K. Händel,<sup>1</sup> Etienne Daum,<sup>1</sup> Benedikt Berlitz,<sup>1</sup> Alexander Bilmes,<sup>1,2</sup> and Alexey V. Ustinov<sup>1</sup>

<sup>1</sup>*Physikalisches Institut, Karlsruhe Institute of Technology, 76131 Karlsruhe, Germany*

<sup>2</sup>*Google Research, Mountain View, CA, USA*

(Dated: 4 March 2026)

**The coherence of superconducting quantum computers is severely limited by material defects that create parasitic two-level-systems (TLS). Progress is complicated by lacking understanding how TLS are created and in which parts of a qubit circuit they are most detrimental. Here, we present a method to determine the individual positions of TLS at the surface of a transmon qubit. We employ a set of on-chip gate electrodes near the qubit to generate local DC electric fields that are used to tune the TLS' resonance frequencies. The TLS position is inferred from the strengths at which TLS couple to different electrodes and comparing them to electric field simulations. We found that the majority of detectable surface-TLS was residing on the leads of the qubit's Josephson junction, despite the dominant contribution of its coplanar capacitor to electric field energy and surface area. This indicates that the TLS density is significantly enhanced near shadow-evaporated electrodes fabricated by lift-off techniques. Our method is useful to identify critical circuit regions where TLS contribute most to decoherence, and can guide improvements in qubit design and fabrication methods.**

## INTRODUCTION

The nature of two-level tunneling systems (TLS) in amorphous materials has been puzzling generations of physicists<sup>1</sup>. Today, TLS are recognized as the primary source of decoherence in superconducting qubits. A type of TLS that was well-studied in glasses is thought to originate in the tunneling of a single or a few atoms between two slightly different locations in the disordered material as illustrated in Fig. 1a<sup>2</sup>. In superconducting circuits, amorphous surface oxides on electrodes and those used for tunnel barriers of qubit junctions are thus a known host for TLS<sup>3-8</sup>. In addition, microfabrication techniques were shown to spoil the crystallinity of the substrate and to leave residuals of glassy photoresist<sup>9-11</sup>. There is a variety of other models of TLS formation, and it remains unknown which types of TLS are limiting qubit coherence<sup>12</sup>. To obtain insight into the elusive microscopic TLS structure, atomistic modeling has gained in importance and was e.g. used to characterize TLS formed by Hydrogen interstitials<sup>13</sup>, by dangling surface atoms<sup>14</sup>, and by tunneling atoms in Josephson junctions<sup>15,16</sup>.

When the tunneling entity carries a charge, TLS defects possess an electric dipole moment by which they couple to the AC electric field of the resonator or qubit mode, and they quickly dissipate resonantly absorbed energy via their strong phonon coupling. Optimizing the circuit design in order to minimize the coupling of TLS to the AC-electric field from the qubit mode is thus a prerequisite for long coherence times<sup>5,17</sup>. The experimental progress currently relies on laborious experiments searching for better materials and improving fabrication procedures<sup>14,17-19</sup>. A standard method is to extract TLS loss in resonators from their power-dependent quality factor. In qubits however, energy relaxation can be dominated by only a few of the most

strongly coupled near-resonant TLS. Moreover, the resonance frequencies of TLS often fluctuate due to their electric dipole or longer-range phonon interaction with thermally activated TLS<sup>20,21</sup>, due to diffusing charge<sup>22</sup>, and due to the impact of high-energy particles which may redistribute the states of neighboring charge traps and bi-stable TLS<sup>23-25</sup>. The resulting fluctuations of qubit resonance frequencies and coherence times<sup>26-28</sup> are especially problematic for quantum processors as they rely on well-calibrated and stable qubits.

The strong interaction of TLS with qubits allows one to characterize them individually<sup>4,29,30</sup>. TLS swap spectroscopy reveals the resonance frequencies of sufficiently strongly coupled TLS by detecting minima in the qubit energy relaxation time  $T_1$  that is measured as a function of qubit frequency<sup>4,31,32</sup>. This method becomes especially powerful when it is combined with means to manipulate the TLS' properties in-situ. Tuning TLS by applied mechanical strain has revealed their interactions with coherent<sup>33</sup> and with thermal<sup>34</sup> TLS, and was used to characterize the TLS' coherent dynamics<sup>35</sup>.

Similarly, TLS were tuned by an applied DC-electric field and individually characterized with superconducting resonators<sup>36-38</sup>. In qubits, E-field tuning allows one to identify whether a TLS is residing in the tunnel barrier of a qubit junction<sup>6</sup>, and provides means to enhance qubit  $T_1$  times<sup>39,40</sup> and their temporal stability<sup>41</sup>. When the tuning electric field can be spatially varied, e.g. by using two independently biased gate electrodes placed above and below the qubit chip, it is possible to obtain information on the circuit interface at which TLS reside<sup>7</sup>. Recently, Hegedüs et al. demonstrated scanning gate microscopy to determine the positions and electric dipole moment orientations of individual TLS at the surface of a superconducting resonator<sup>42</sup>.

Here, we demonstrate a method to generate maps of the locations of individual TLS on the surface of a transmon qubit. The TLS locations are inferred from their measured

\*Corresponding author: juergen.lisenfeld@kit.edu

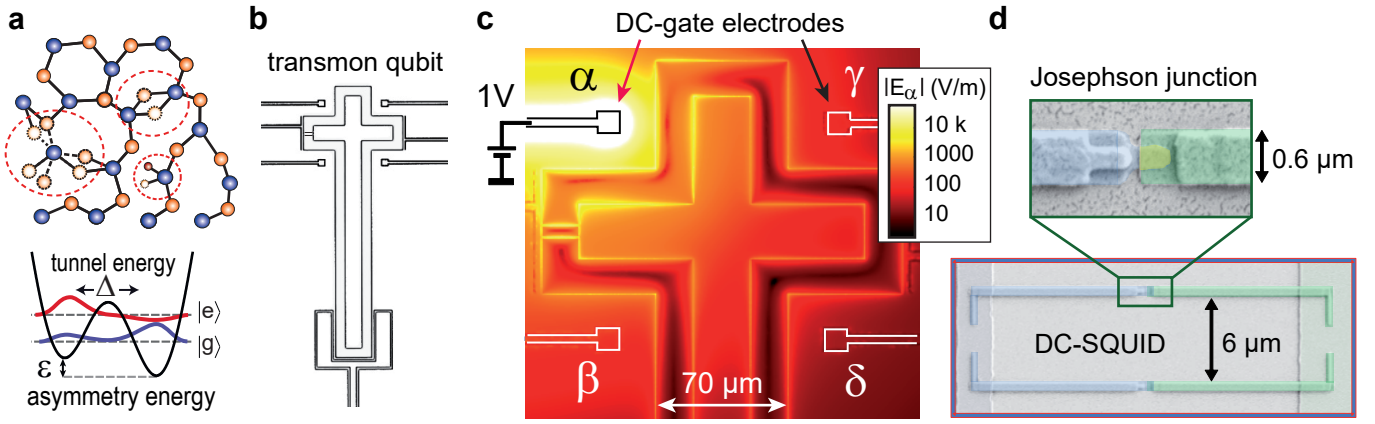


FIG. 1. **Qubit design to measure TLS locations.** **a** Models of Two-Level-Systems (TLS) formed by delocalized atoms in an amorphous material, and corresponding TLS double-well potential that is characterized by the tunneling energy  $\Delta$  between the TLS states and the asymmetry energy  $\varepsilon$ . **b** Layout of the transmon qubit, formed by a cross-shaped island that is connected via two Josephson junctions to the surrounding ground plane. **c** Four electrodes indicated by  $\alpha$  to  $\delta$  are placed around the qubit to generate locally concentrated DC-electric fields. The color encodes the simulated magnitude of the DC-electric field at the sample surface when 1V is applied to electrode  $\alpha$ . **d** False-colored SEM picture of the DC-SQUID and a single Josephson junction.

coupling strengths to each of four on-chip gate electrodes that are placed around the qubit, realizing a method of trilateration. The majority of all detected surface-TLS were found to reside near the leads of the Josephson junctions. Considering the dominant contribution of the qubit's planar capacitor and ground plane to surface area and electric field energy, this result indicates that the TLS density is enhanced at shadow-evaporated electrodes that are deposited by additive lift-off techniques, in contrast to subtractive etching.

## METHODS

### Qubit sample

The transmon qubit sample, shown in Figs 1 b-d, is based on the *XMon*-design by Barends et al.<sup>4</sup> and consists of a DC-SQUID and a cross-shaped island that forms a shunt capacitor with the surrounding ground plane. In addition, the design integrates four gate electrodes labeled  $\alpha$ ... $\delta$  in vicinity of the qubit island which are used to tune the TLS by local DC-electric fields.

The simulated E-field strength  $E_\alpha$  when a voltage of 1V is applied to the  $\alpha$ -electrode is shown by color in Fig. 1 c. Due to the large spatial E-field gradient, the response of a TLS depends sensitively on its distance to the gate electrode. The TLS position can thus be estimated by measuring its tuning strengths to different electrodes and comparing them to the simulated strengths of the local electric fields.

The qubit was fabricated from aluminum on a sapphire substrate, using optical lithography and dry etching for the ground plane and qubit island, and eBeam-patterned Dolan bridges to form the tunnel junctions and their leads (shown in Fig. 1d) in a 3-angle shadow evaporation process that avoids unwanted stray junctions<sup>43</sup>. Details on sample fabrication

and circuit parameters are found in Supplementary Note A. The sample was cooled to a temperature of 25 - 30 mK and measured in a standard setup as detailed in Supplementary Note B.

The qubit showed energy relaxation times  $T_1$  between 5 to 8  $\mu$ s at operation frequencies between 5 and 5.5 GHz. Similarly fabricated qubits without on-chip gate electrodes achieved only slightly longer  $T_1$ -times between 10 and 20  $\mu$ s<sup>39,43</sup>, and these were mostly limited by TLS near circuit electrodes<sup>6,44</sup>. However, the observed  $T_1$ -time falls within the estimate range of the radiative loss via the capacitive coupling to the four electrodes, which were placed in close vicinity to the qubit island to enhance the spatial resolution in TLS localization. This loss channel can be mitigated with an improved design of the qubit and on-chip electrodes<sup>45</sup>. Further details on loss are discussed in Supplementary Note C.

### TLS spectroscopy

The resonance frequency of a charged TLS is given by the hyperbolic function

$$\omega_{\text{TLS}} = \sqrt{\Delta^2 + (\varepsilon + 2\mathbf{p} \cdot \mathbf{E})^2} / \hbar, \quad (1)$$

where  $\Delta$  is the tunneling energy between its two states, and  $\varepsilon$  is a background asymmetry energy of the TLS' double-well potential (see Fig. 1 a) that depends on local static electric and strain fields. In addition, the asymmetry energy is tuned by the component of the applied E-field  $\mathbf{E}$  at the position of the TLS that is parallel to the TLS' electric dipole moment  $\mathbf{p}$ . In our experiments, the E-field  $\mathbf{E} = \mathbf{E}_\alpha + \mathbf{E}_\beta + \mathbf{E}_\gamma + \mathbf{E}_\delta$  is controlled via the applied voltages  $V_\alpha$ ... $V_\delta$  on the four gate electrodes.

We detect TLS resonances using the TLS swap-spectroscopy protocol<sup>4,6,33</sup> depicted in the top inset of Fig. 2a. The qubit

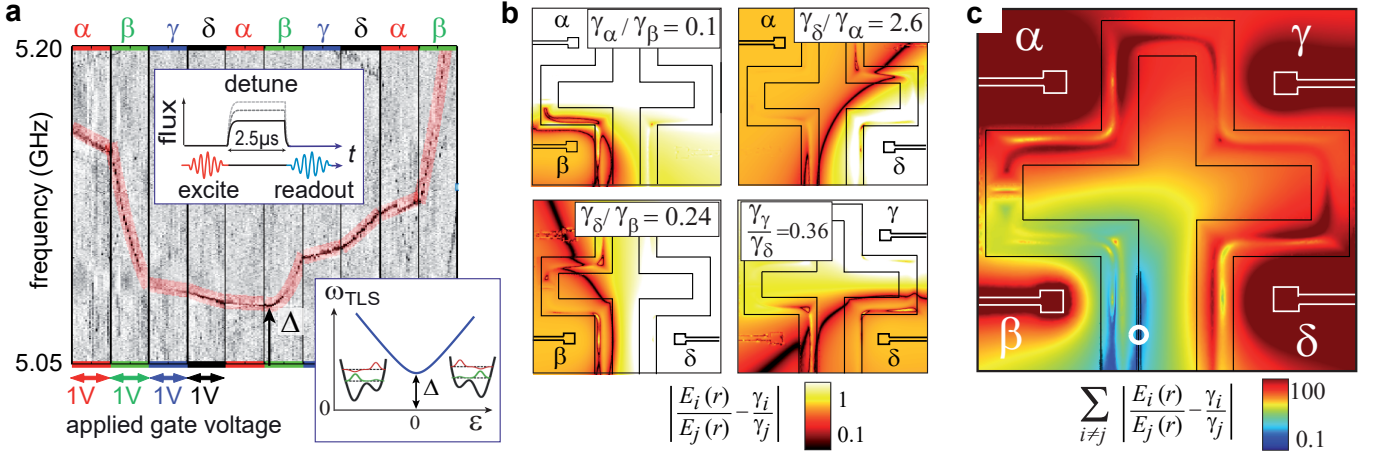


FIG. 2. **Finding the location of a TLS.** **a** TLS spectroscopy using the protocol in the inset, to reveal the resonance frequencies of TLS from minima (dark pixels) in the resulting qubit population  $P(|1\rangle)$ . In each segment, the voltage on a different electrode  $\alpha\dots\delta$  is increased by 1V. The highlighted trace shows a TLS as it is tuned through its symmetry point (arrow) according to Eq. (1) as illustrated in the lower inset. The TLS' response strengths  $\gamma_i$  to the different electrodes are obtained by fitting such traces to Eq. (1), and provide information about the TLS' distance to the electrodes. **b** Difference between the measured TLS response strength ratio  $\gamma_i/\gamma_j$  and the corresponding simulated E-field ratio (colorscale) for the TLS observed in **a**. Minima (dark pixels) indicate possible TLS positions. Each panel shows data from a different electrode pair as marked in the legends together with the measured tuning ratio. **c** The colorscale shows the difference sum  $\sigma$  (Eq. 3) over all 6 unique combinations of electrode pairs. The minimum (white circle) marks the most probable TLS position.

is excited by a microwave  $\pi$ -pulse and tuned to one of various probe frequencies for a duration of  $2.5\mu\text{s}$  to allow for interactions with TLS. The remaining qubit excitation  $P_{|1\rangle}$  then provides an estimate for the qubit  $T_1$  time at the probe frequency<sup>39</sup>, which shows a minimum when the qubit is in resonance with a sufficiently strongly coupled TLS.

To measure the TLS' coupling strengths to the four DC-electrodes, their resonances are traced by TLS spectroscopy while the voltages on the DC-electrodes are swept. As an example, Figure 2a shows the resonance of a TLS that was tuned through the symmetry point of its hyperbola Eq. (1), where in each segment the voltage on the indicated gate electrode  $\alpha\dots\delta$  was stepwise increased by 1V while other voltages were kept constant. The slope of the hyperbola in the different segments then depends on the tuning strength of the TLS by the corresponding electrode. It is obtained by fitting such traces to Eq. (1), where the factor for the induced asymmetry energy  $2\mathbf{p}\cdot\mathbf{E}$  is replaced by  $\sum_i \gamma_i V_i$ . Here,  $i \in \{\alpha, \beta, \gamma, \delta\}$  indicates the electrode that is biased by the voltage  $V_i$ , and  $\gamma_i$  are the fitting tuning strengths that contain information on the distance of the TLS to the corresponding electrodes.

### TLS localization

Possible locations of the TLS could in principle be inferred from the measured tuning strengths by searching for positions  $(x,y)$  where the simulated electric field  $\mathbf{E}_i(x,y)$  fulfills the equation  $2\mathbf{p}\cdot\mathbf{E}_i(x,y) = \gamma_i V_i$ . However, this would require knowledge of the TLS' electric dipole moment  $\mathbf{p}$  and its orientation relative to the local E-field. In our analysis, we therefore consider only relative tuning strengths of the TLS by

different electrodes, and search for positions  $(x,y)$  fulfilling the equations

$$\frac{2\mathbf{p}\cdot\mathbf{E}_i(x,y)}{2\mathbf{p}\cdot\mathbf{E}_j(x,y)} = \frac{\gamma_i V_i}{\gamma_j V_j}, \text{ where } \{i \neq j\} \in \alpha, \beta, \gamma, \delta. \quad (2)$$

In these equations, the TLS' electric dipole moment  $\mathbf{p}$  can be eliminated given that the two fields  $\mathbf{E}_i$  and  $\mathbf{E}_j$  have parallel orientation at the position of the TLS. In the following, we argue that this is indeed the case in our experiment, because we are detecting only TLS in close vicinity to the edges of qubit electrodes where all electric fields are sufficiently aligned.

To be able to detect a TLS in qubit  $T_1$ -swap-spectroscopy, its (resonant) coupling strength to the qubit  $g = \left(\frac{\Delta}{\hbar\omega_{\text{TLS}}}\right) \mathbf{p}\cdot\mathbf{E}_{\text{rms}}$  must be large enough to result in a measurable decrease of the qubit's energy relaxation rate. Thus, TLS can only be detected in circuit regions where the qubit's AC-electric field strength  $|E_{\text{rms}}|$  exceeds  $g_{\text{min}}/p_{\parallel}$ . Assuming  $\Delta/\hbar\omega_{\text{TLS}} \approx 1$  (most strongly coupled TLS near their symmetry point) and a field-parallel dipole moment of  $p_{\parallel} \approx 1e\text{\AA}$ <sup>3,4,37,46</sup>, the required minimum coupling strength  $g_{\text{min}}$  can be estimated from the energy relaxation rate of the resonantly coupled qubit-TLS system<sup>4</sup>  $\Gamma_1 = 2(g_{\text{min}}/\hbar)^2/\Gamma + \Gamma_{1,Q}$ , where  $\Gamma_{1,Q}$  is the energy relaxation rate of the isolated qubit, and  $\Gamma = \Gamma_{1,\text{TLS}}/2 + \Gamma_{2,\text{TLS}} + \Gamma_{1,Q}/2 + \Gamma_{2,Q}$  is the sum of TLS and qubit energy relaxation and dephasing rates. The assumption that TLS are detected if they reduce the qubit's  $T_1$  time by a factor of  $\kappa$  translates into a minimum coupling strength of  $g_{\text{min}} = \hbar\sqrt{\kappa\cdot\Gamma_{1,Q}\Gamma}/2$  and corresponding minimum AC-electric qubit field strength  $E_{\text{min}} = g_{\text{min}}/p_{\parallel}$ . A plot of these relations can be found in Supplementary Note E. For

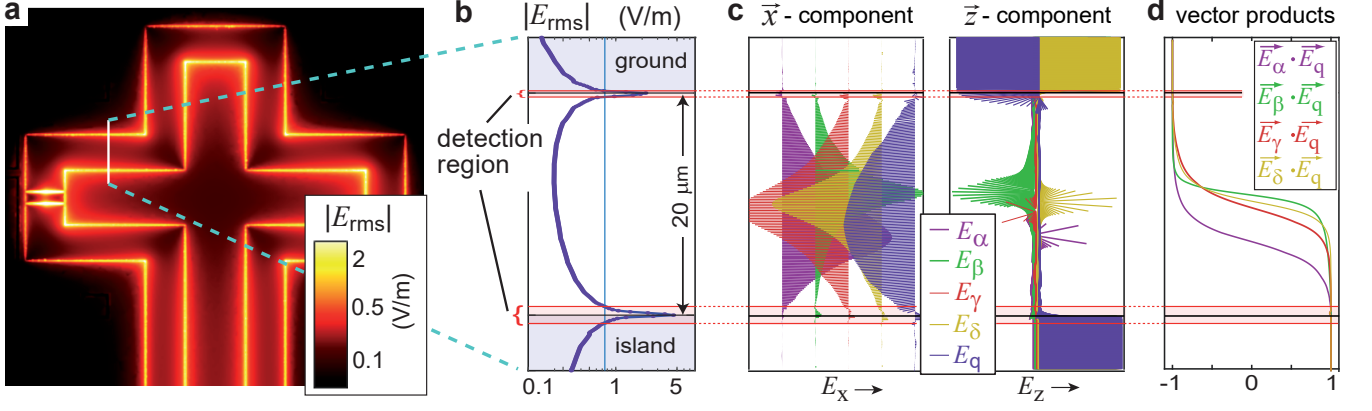


FIG. 3. **Strength and orientations of AC- and DC-electric fields.** **a** Magnitude of the qubit’s AC-electric field  $|E_{\text{rms}}|$  as simulated with Ansys HFSS. **b** Cross-section of  $|E_{\text{rms}}|$  along the white line in **a**. TLS can only be detected in the red shaded area where the field exceeds a minimum strength  $E_{\text{min}}$  (blue vertical line). **c** Components of the electric fields from the four electrodes and the qubit, plotted in  $\bar{x}$ - and  $\bar{z}$  directions (left and right panel). Near the center of the gap between ground plane and qubit island, the fields induced by the gate electrodes change their direction and point in different directions. **d** The normalized vector product between the fields of gate electrodes and the qubit approaches unity near the electrode edges where all fields point in the same direction.

a qubit  $T_1 = 7 \mu\text{s}$ , TLS coherence times in the range of  $T_{1,\text{TLS}} \approx T_{2,\text{TLS}} \approx 0.1 - 2 \mu\text{s}$ <sup>4,6,33,47-49</sup>, and  $\kappa = 5\%$ , we find a  $E_{\text{min}}$  range of  $\approx 0.3 - 3 \text{ V/m}$ .

Figure 3a shows the simulated magnitude of the qubit’s AC-electric field  $|E_{\text{rms}}|$ . A cross section through the edges of ground plane and qubit island is shown in Fig 3b and illustrates that in our qubit sample, TLS can only be detected within an  $\approx 1 - 2 \mu\text{m}$  distance from the edge of qubit electrodes where  $|E_{\text{rms}}| > E_{\text{min}}$ . Since  $E_{\text{min}}$  decreases with the square root of the qubit’s  $T_1$  time, more coherent qubits are affected by TLS in a wider area which includes more weakly coupled ones as illustrated in Supplementary Note E.

To show that the electric fields from different on-chip electrodes are indeed sufficiently parallel, such that the dipole moment in Eq. (2) can be canceled in order to simplify the solution for possible TLS positions, in Fig. 3c we plot the electric fields’  $\bar{x}$ - and  $\bar{z}$ -components along the white line in Fig. 3a. Near the center of the gap between ground and qubit island, the E-fields point in different directions. However, within the short distance to the electrode edges where TLS are detected in our experiment, all E-fields are well aligned since their vector products with the qubit field  $\vec{E}_q$  approach unity as plotted in Fig. 3d. This is also the case near the junction leads as shown in Supplementary Note E.

After dropping the TLS’ electric dipole moment  $\mathbf{p}$  in the vector product in Eq. (2), we find the most probable TLS position  $(x, y)$  by minimizing the sum of residuals

$$\sigma = \sum_{i \neq j} \left| \frac{E_i(x, y)}{E_j(x, y)} - \frac{\gamma_i}{\gamma_j} \right|, \text{ where } \{i \neq j\} \in \alpha, \beta, \gamma, \delta. \quad (3)$$

Each of the six summands in Eq. (3) is the difference between the measured tuning ratio of two electrodes with the corresponding simulated E-field ratio at position  $(x, y)$ . Figure 2b shows exemplarily the contribution of four summands for the TLS observed in Fig. 2a, where minima

(dark pixels) indicate possible TLS positions that are confined along approximate circles centered at the electrode which is nearest to the TLS. For example, the TLS shown in Fig. 2a shows a 10 times stronger response to the  $\beta$ -electrode than the  $\alpha$ -electrode. This places possible TLS positions in vicinity of the  $\beta$ -electrode as shown in the top left panel of Fig. 2b.

Figure 2c shows a plot of the complete difference sum of Eq. (3) that contains information from all six electrode pairs, and where the global minimum (marked by a white circle) then indicates the most likely TLS position. In this analysis, we allow only solutions of TLS positions within the region where the qubit’s AC field is strong enough ( $|E_{\text{rms}}| > E_{\text{min}}$ ) so that TLS can be detected.

## RESULTS

### TLS distribution

To generate a map of the individual TLS positions on the qubit circuit, we swept the voltages on each of the four electrodes in a range between  $-60\text{V}$  and  $+100\text{V}$  and performed TLS spectroscopy in a  $150\text{-MHz}$  wide window as shown in Fig. 2a. In total, 55 TLS were observed in a single qubit sample whose tuning strengths to all four electrodes could be characterized (see Supplementary Note F for further details). For the analysis, TLS were discarded whose coupling strength to the upper electrodes  $\alpha$  and  $\gamma$  were indistinguishable from zero so that their location could not be precisely determined. This is the case for TLS that reside on the long arm of the qubit island (see Fig. 1b).

The determined individual TLS positions are marked by yellow circles in Fig 4a. The majority of TLS (58%) were found to reside at the leads of the qubit’s Josephson junctions. Near the edges of the qubit island and the ground plane, 25% and 16% were found, respectively. In this example, a

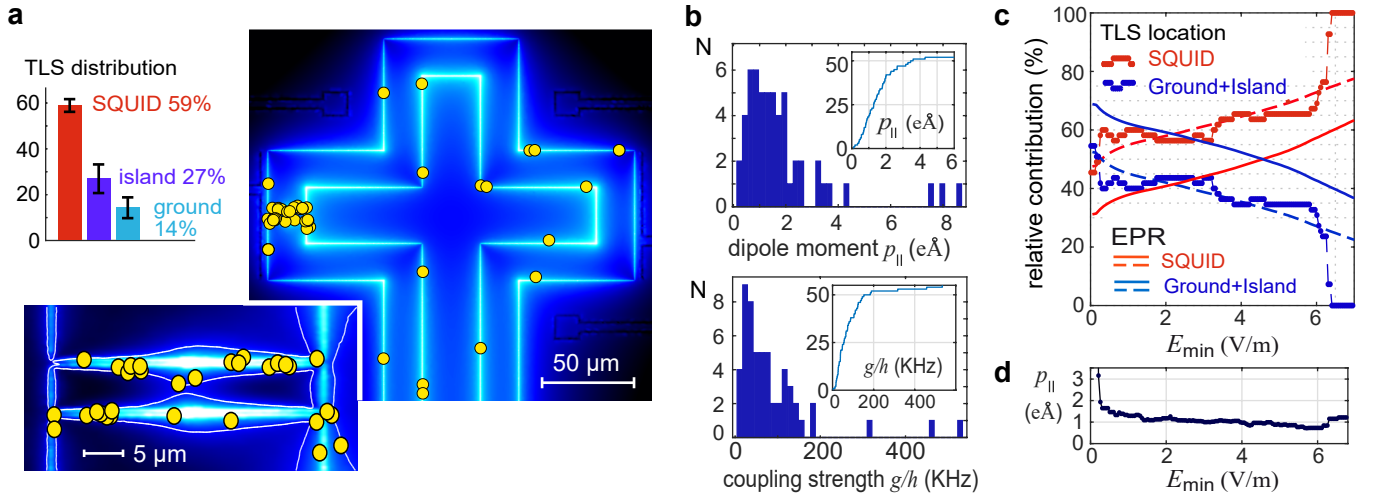


**FIG. 4. TLS locations and properties.** **a** Map of the individual positions of detected surface-TLS (yellow circles). Most TLS ( $\approx 59\%$ ) were found at the Josephson junctions leads (see lower inset for a zoom on the DC-SQUID). Near the edges of capacitor island and ground plane, 27% and 14% of TLS were identified, respectively. **b** Histograms and cumulative distributions (insets) of the TLS' electric dipole moment component  $p_{||}$  (upper panel) and TLS-qubit coupling strengths  $g/h$  (lower panel) as estimated from the TLS' positions, their coupling strengths to the electrodes, and the local magnitude of the qubit AC field  $E_{rms}$ . **c** Percentage of TLS identified on the SQUID vs. ground plane plus island, plotted as a function of the electric field threshold  $E_{min}$  that accounts for TLS observability in swap spectroscopy. The solid lines are the energy participation ratios (EPRs) of the SQUID (red) and the ground plus island (blue) in regions where  $E_{rms} > E_{min}$ . The dashed lines are a fit of these ratios to the observed TLS distribution, obtained by assuming that the TLS density in the SQUID area is enhanced by a factor of 2. **d** Determined median TLS electric dipole moment  $p_{||}$  as a function of  $E_{min}$ .

relatively small value of  $E_{min} = 0.75$  V/m was chosen as the threshold field above which TLS can be detected, which limits the area of allowed TLS positions to the thin white line in the inset of Fig. 4a.

To check the mapping procedure's reliability, the analysis is repeated for various values of  $E_{min}$ . The resulting percentages of TLS found on the SQUID leads vs. those on the qubit island and ground plane are plotted in Fig. 4c. These remain at a ratio of 60:40 within the most probable range of  $E_{min} \approx 0.3..3$  V/m as estimated above, which backs the robustness of the method. Above a value of  $E_{min} \approx 6$  V/m, the procedure fails since it is forced to place all TLS on the DC-SQUID. For the given data and qubit sample, we estimate an uncertainty in the TLS positions of about  $6 \mu\text{m}$  as further discussed in Supplementary Note G. This resolution can be enhanced with more suitable qubit designs that avoid sharp corners.

### Excess TLS density near the SQUID

Notably, the observed TLS distribution points towards an excess density of TLS near the DC-SQUID leads. Since the probability to detect a surface-TLS scales with the square of the local qubit field, the expected ratio of the numbers of TLS observed near the SQUID vs. ground plane and qubit island can be estimated by comparing their energy participation ratios (EPRs). By calculating the EPR, we limit the integrals over  $|E_{rms}|^2$  to regions where  $E_{rms} > E_{min}$  to account for TLS detectability in swap spectroscopy, which sets this calculation apart from the common participation ratio analysis<sup>5</sup> that

includes also weakly coupled TLS. Further details are given in Supplementary Note E. The result is plotted with solid red and blue lines in Fig. 4c, and predicts that most TLS ( $>50\%$ ) would be observed on either the qubit island or ground plane in the whole range of reasonable values  $E_{min} < 4$  V/m, in stark contrast to the experimental data.

This finding can be reconciled assuming that the TLS density near the DC SQUID is about two times larger than near qubit island and ground plane, presumably due to its different fabrication procedure. The expected TLS distribution for this case is shown by the dashed red and blue lines in Fig. 4c, which are obtained by scaling the electric field energy  $E_{rms}^2$  integrated over the SQUID area by a factor of two. We find a very good agreement with the experimental result that is mostly insensitive to the choice of  $E_{min}$  in the mapping algorithm.

From the TLS' estimated positions, we can calculate their electric dipole moments using the measured tuning strengths  $\gamma_i$  and the simulated local E-fields of corresponding DC-gate electrodes. Similarly, the TLS' coupling strength to the qubit  $g$  can be estimated using the simulation of the qubit's AC-electric field strength at the TLS' position. Figure 4b shows their histograms and cumulative distributions for the representative example shown in Fig. 4a. The extracted median TLS dipole moment varies weakly with  $E_{min}$  as shown in Fig. 4d, and is estimated to  $p_{||} \approx 1.12 \pm 0.12 e\text{\AA}$  which is well in accordance with results obtained using other methods in qubits and lumped-element resonators<sup>3,4,37</sup>.

## DISCUSSION

We have demonstrated a method to determine the individual positions and electric dipole moments of TLS defects in a transmon qubit. The majority ( $\approx 58\%$ ) of observed strongly interfering TLS in the qubit sample were found to reside on the qubit's DC-SQUID. This confirms that the leads of tunnel junctions, due to their large electric energy participation, are a critical component which can dominate qubit loss<sup>49–51</sup>. This advocates for the use of wire-tapering techniques to dilute the electric field<sup>52</sup>, and to minimize the size of lift-off structures.

Our results additionally indicate that the TLS density near the junction leads is enhanced by a factor of  $\approx 2$ . This may be attributed to their different fabrication technique as compared to the qubit capacitor, which can promote TLS formation in various ways. For example, junction formation by shadow evaporation and electron-beam lithography is associated with larger amounts of resist residuals and enhanced roughness of junction lead interfaces<sup>10,11,53</sup>. The junctions were fabricated with a lift-off process which reportedly leaves excess residues<sup>9,51</sup>. Also, thinner films showed a larger density of grain boundaries associated with enhanced oxygen diffusion<sup>19</sup>.

The technique to find TLS positions works with various (charge-resilient) qubit types such as flux and phase or transmon qubits, and provides information on the local TLS density in a single sample without the need to average over a large ensemble of differently designed qubits. It can be applied to arbitrary qubit designs when the grid of DC-electrodes is patterned on a wafer placed above the qubits in a flip-chip configuration. This is similar to the recently demonstrated scanning gate spectroscopy<sup>42</sup>, but does not require mechanical control.

Control over the local DC-electric field also enables one to actively suppress decoherence by tuning dominating TLS defects out of the qubit resonance<sup>39–41</sup>. For this, multiple electrodes provide independent control over TLS at different locations which enhances the ability to decouple the qubit from the decohering bath.

The current method cannot determine at which interfaces TLS are residing. This is possible with additional gate electrode placed above and below the qubit chip, allowing one to also distinguish TLS located at the metal-substrate interface from those at the metal-air interface and the substrate as we showed in previous work<sup>7</sup>. Moreover, the combination with TLS tuning by applied mechanical strain provides additional information of TLS densities in tunnel junction barriers<sup>6</sup>, and is useful to enhance the numbers of observable TLS in a given qubit circuit.

Our method opens door to study TLS formation due to fabrication techniques and contaminants, for example by comparing TLS densities in differently processed areas of the same qubit circuit. This approach can serve to guide improvements in qubit fabrication and design, which is vitally needed for the advancement of large-scale superconducting quantum processors where TLS defects present a major obstacle.

## DATA AVAILABILITY

The raw data that support the findings of this study are available from the public repository Zenodo, DOI:10.5281/zenodo.18847452.

## ACKNOWLEDGEMENTS

We thank Hannes Rotzinger for his support with the experimental setup and fruitful discussions, and Lukas Radtke for his commitment to the clean-room and help with sample fabrication. This work was funded by Google, which is gratefully acknowledged.

## AUTHOR CONTRIBUTION

J.L. conceived and supervised the project and wrote the manuscript. E-field tuning techniques were developed by J.L. and A.B. Data was acquired and analyzed by J.L. with support from A.K.H. and B.B. The sample was fabricated by A.K.H. and A.B. Simulations were done by A.K.H., E.D. and B.B. The experimental infrastructure was provided by A.V.U. All authors contributed to discussion and the final manuscript.

## COMPETING INTERESTS

The authors declare no competing financial or non-financial interests.

## REFERENCES

- <sup>1</sup>C Yu Clare and Hervé M Carruzzo. Two-level systems and the tunneling model: A critical view. *Low-temperature Thermal And Vibrational Properties Of Disordered Solids: A Half-century Of Universal "Anomalies" Of Glasses*, page 113, 2022.
- <sup>2</sup>Christian Enss and Siegfried Hunklinger. *Low-temperature physics*, chapter 9. Springer, Berlin, Heidelberg, 2005.
- <sup>3</sup>John M. Martinis, K. B. Cooper, R. McDermott, Matthias Steffen, Markus Ansmann, K. D. Osborn, K. Cicak, Seongshik Oh, D. P. Pappas, R. W. Simmonds, and Clare C. Yu. Decoherence in josephson qubits from dielectric loss. *Phys. Rev. Lett.*, 95:210503, Nov 2005.
- <sup>4</sup>R. Barends, J. Kelly, A. Megrant, D. Sank, E. Jeffrey, Y. Chen, Y. Yin, B. Chiaro, J. Mutus, C. Neill, P. O'Malley, P. Roushan, J. Wenner, T. C. White, A. N. Cleland, and John M. Martinis. Coherent josephson qubit suitable for scalable quantum integrated circuits. *Physical Review Letters*, 111(8), August 2013.
- <sup>5</sup>C. Wang, C. Axline, Y. Y. Gao, T. Brecht, Y. Chu, L. Frunzio, M. H. Devoret, and R. J. Schoelkopf. Surface participation and dielectric loss in superconducting qubits. *Appl. Phys. Lett.*, 107(16), 2015.
- <sup>6</sup>Jürgen Lisenfeld, Alexander Bilmes, Anthony Megrant, Rami Barends, Julian Kelly, Paul Klimov, Georg Weiss, John M. Martinis, and Alexey V. Ustinov. Electric field spectroscopy of material defects in transmon qubits. *npj Quantum Information*, 5(1), November 2019.
- <sup>7</sup>Alexander Bilmes, Anthony Megrant, Paul Klimov, Georg Weiss, John M. Martinis, Alexey V. Ustinov, and Jürgen Lisenfeld. Resolving the positions of defects in superconducting quantum bits. *Scientific Reports*, 10(1), February 2020.
- <sup>8</sup>Nathalie P De Leon, Kohei M Itoh, Dohun Kim, Karan K Mehta, Tracy E Northup, Hanhee Paik, BS Palmer, Nitin Samarth, Sorawis Sangtawesin, and David W Steuerman. Materials challenges and opportunities for quantum computing hardware. *Science*, 372(6539):eabb2823, 2021.

- <sup>9</sup>C. M. Quintana, A. Megrant, Z. Chen, A. Dunsworth, B. Chiaro, R. Barends, B. Campbell, Yu Chen, I.-C. Hoi, E. Jeffrey, J. Kelly, J. Y. Mutus, P. J. J. O'Malley, C. Neill, P. Roushan, D. Sank, A. Vainsencher, J. Wenner, T. C. White, A. N. Cleland, and John M. Martinis. Characterization and reduction of microfabrication-induced decoherence in superconducting quantum circuits. *Applied Physics Letters*, 105(6), August 2014.
- <sup>10</sup>A Dunsworth, A Megrant, C Quintana, Zijun Chen, R Barends, B Burkett, B Foxen, Yu Chen, B Chiaro, A Fowler, et al. Characterization and reduction of capacitive loss induced by sub-micron josephson junction fabrication in superconducting qubits. *Applied Physics Letters*, 111(2), 2017.
- <sup>11</sup>Michael A Gingras, Bethany M Niedzielski, Kevin A Grossklaus, Duncan Miller, Felipe Contipelli, Kate Azar, Luke D Burkhart, Gregory Calusine, Daniel Davis, Renée DePencier Piñero, et al. Improving transmon qubit performance with fluorine-based surface treatments. *arXiv preprint arXiv:2507.08089*, 2025.
- <sup>12</sup>Clemens Müller, Jared H Cole, and Jürgen Lisenfeld. Towards understanding two-level-systems in amorphous solids: insights from quantum circuits. *Reports on Progress in Physics*, 82(12):124501, 2019.
- <sup>13</sup>Aaron M Holder, Kevin D Osborn, CJ Lobb, and Charles B Musgrave. Bulk and surface tunneling hydrogen defects in alumina. *Physical review letters*, 111(6):065901, 2013.
- <sup>14</sup>Zhe Wang, Clare C Yu, and Ruqian Wu. Why superconducting ta qubits have fewer tunneling two-level systems at the vacuum-oxide interface than nb qubits. *Physical Review Applied*, 23(2):024017, 2025.
- <sup>15</sup>Timothy C DuBois, Manolo C Per, Salvy P Russo, and Jared H Cole. Delocalized oxygen as the origin of two-level defects in josephson junctions. *Physical review letters*, 110(7):077002, 2013.
- <sup>16</sup>Alejandro Pérez Paz, Irina V Lebedeva, Ilya V Tokatly, and Angel Rubio. Identification of structural motifs as tunneling two-level systems in amorphous alumina at low temperatures. *Physical Review B*, 90(22):224202, 2014.
- <sup>17</sup>Suhaj Ganjam, Yanhao Wang, Yao Lu, Archan Banerjee, Chan U Lei, Lev Krayzman, Kim Kisslinger, Chenyu Zhou, Ruoshui Li, Yichen Jia, et al. Surpassing millisecond coherence in on chip superconducting quantum memories by optimizing materials and circuit design. *Nature Communications*, 15(1):3687, 2024.
- <sup>18</sup>Conal E Murray. Material matters in superconducting qubits. *Materials Science and Engineering: R: Reports*, 146:100646, 2021.
- <sup>19</sup>Janka Biznárová, Amr Osman, Emil Rehman, Lert Chayanun, Christian Križan, Per Malmberg, Marcus Rommel, Christopher Warren, Per Delsing, August Yurgens, et al. Mitigation of interfacial dielectric loss in aluminum-on-silicon superconducting qubits. *npj Quantum Information*, 10(1):78, 2024.
- <sup>20</sup>Lara Faoro and Lev B Ioffe. Interacting tunneling model for two-level systems in amorphous materials and its predictions for their dephasing and noise in superconducting microresonators. *Physical Review B*, 91(1):014201, 2015.
- <sup>21</sup>Clemens Müller, Jürgen Lisenfeld, Alexander Shnirman, and Stefano Poletto. Interacting two-level defects as sources of fluctuating high-frequency noise in superconducting circuits. *Physical Review B*, 92(3):035442, 2015.
- <sup>22</sup>Alexander Bilmes, Sebastian Zanker, Andreas Heimes, Michael Marthaler, Gerd Schön, Georg Weiss, Alexey V Ustinov, and Jürgen Lisenfeld. Electronic decoherence of two-level systems in a josephson junction. *Physical review B*, 96(6):064504, 2017.
- <sup>23</sup>Matt McEwen, Lara Faoro, Kunal Arya, Andrew Dunsworth, Trent Huang, Seon Kim, Brian Burkett, Austin Fowler, Frank Arute, Joseph C Bardin, et al. Resolving catastrophic error bursts from cosmic rays in large arrays of superconducting qubits. *Nature Physics*, 18(1):107–111, 2022.
- <sup>24</sup>Ted Thorbeck, Andrew Eddins, Isaac Lauer, Douglas T McClure, and Malcolm Carroll. Two-level-system dynamics in a superconducting qubit due to background ionizing radiation. *PRX Quantum*, 4(2):020356, 2023.
- <sup>25</sup>Elia Bertoldo, Victor Pérez Sánchez, Maria Martinez, Manel Martinez, Hawraa Khalife, and Pol Forn Diaz. Cosmic muon flux attenuation methods for superconducting qubit experiments. *New Journal of Physics*, 2023.
- <sup>26</sup>Paul V Klimov, Julian Kelly, Zijun Chen, Matthew Neeley, Anthony Megrant, Brian Burkett, Rami Barends, Kunal Arya, Ben Chiaro, Yu Chen, et al. Fluctuations of energy-relaxation times in superconducting qubits. *Physical review letters*, 121(9):090502, 2018.
- <sup>27</sup>Jonathan J Burnett, Andreas Bengtsson, Marco Scigliuzzo, David Niepce, Marina Kudra, Per Delsing, and Jonas Bylander. Decoherence benchmarking of superconducting qubits. *npj Quantum Information*, 5(1):54, 2019.
- <sup>28</sup>Steffen Schlör, Jürgen Lisenfeld, Clemens Müller, Alexander Bilmes, Andre Schneider, David P. Pappas, Alexey V. Ustinov, and Martin Weides. Correlating decoherence in transmon qubits: Low frequency noise by single fluctuators. *Phys. Rev. Lett.*, 123:190502, Nov 2019.
- <sup>29</sup>John M Martinis, Ken B Cooper, Robert McDermott, Matthias Steffen, Markus Ansmann, KD Osborn, Katarina Cicak, Seongshik Oh, David P Pappas, Raymond W Simmonds, et al. Decoherence in josephson qubits from dielectric loss. *Physical review letters*, 95(21):210503, 2005.
- <sup>30</sup>Matthew Neeley, Markus Ansmann, Radoslaw C Bialczak, Max Hofheinz, Nadav Katz, Erik Lucero, A O'connell, Haohua Wang, Andrew N Cleland, and John M Martinis. Process tomography of quantum memory in a josephson-phase qubit coupled to a two-level state. *Nature Physics*, 4(7):523–526, 2008.
- <sup>31</sup>Amr Osman, Jorge Fernández-Pendás, Christopher Warren, Sandoko Kosen, Marco Scigliuzzo, Anton Frisk Kockum, Giovanna Tancredi, Anita Fadavi Roudsari, and Jonas Bylander. Mitigation of frequency collisions in superconducting quantum processors. *Physical Review Research*, 5(4):043001, 2023.
- <sup>32</sup>Dante Colao Zanuz, Quentin Ficheux, Laurent Michaud, Alexei Orekhov, Kilian Hanke, Alexander Flasby, Mohsen Bahrami Panah, Graham J Norris, Michael Kerschbaum, Ants Remm, et al. Mitigating losses of superconducting qubits strongly coupled to defect modes. *Physical Review Applied*, 23(4):044054, 2025.
- <sup>33</sup>Jürgen Lisenfeld, Grigoriy J. Grabovskij, Clemens Müller, Jared H. Cole, Georg Weiss, and Alexey V. Ustinov. Observation of directly interacting coherent two-level systems in an amorphous material. *Nature Comm.*, 6:6182, 2015.
- <sup>34</sup>Saskia M Meißner, Arnold Seiler, Jürgen Lisenfeld, Alexey V Ustinov, and Georg Weiss. Probing individual tunneling fluctuators with coherently controlled tunneling systems. *Physical Review B*, 97(18):180505, 2018.
- <sup>35</sup>Jürgen Lisenfeld, Alexander Bilmes, Shlomi Matityahu, Sebastian Zanker, Michael Marthaler, Moshe Schechter, Gerd Schön, Alexander Shnirman, Georg Weiss, and Alexey V Ustinov. Decoherence spectroscopy with individual two-level tunneling defects. *Scientific reports*, 6(1):23786, 2016.
- <sup>36</sup>Bahman Sarabi, Aruna N Ramanayaka, Alexander L Burin, Frederick C Wellstood, and Kevin D Osborn. Projected dipole moments of individual two-level defects extracted using circuit quantum electrodynamics. *Physical review letters*, 116(16):167002, 2016.
- <sup>37</sup>Chih-Chiao Hung, Liuqi Yu, Neda Foroozani, Stefan Fritz, Dagmar Gerthsen, and Kevin D. Osborn. Probing hundreds of individual quantum defects in polycrystalline and amorphous alumina. *Physical Review Applied*, 17(3), March 2022.
- <sup>38</sup>SE De Graaf, Sumedh Mahashabde, SE Kubatkin, A Ya Tzalenchuk, and AV Danilov. Quantifying dynamics and interactions of individual spurious low-energy fluctuators in superconducting circuits. *Physical Review B*, 103(17):174103, 2021.
- <sup>39</sup>Jürgen Lisenfeld, Alexander Bilmes, and Alexey V Ustinov. Enhancing the coherence of superconducting quantum bits with electric fields. *npj Quantum Information*, 9(1):8, 2023.
- <sup>40</sup>Larry Chen, Kan-Heng Lee, Chuan-Hong Liu, Brian Marinelli, Ravi K Naik, Ziqi Kang, Noah Goss, Hyunseong Kim, David I Santiago, and Irfan Siddiqi. Scalable and site-specific frequency tuning of two-level system defects in superconducting qubit arrays. *arXiv preprint arXiv:2503.04702*, 2025.
- <sup>41</sup>Andrew Dane, Karthik Balakrishnan, Brent Wacaser, Li-Wen Hung, HJ Mamin, Daniel Rugar, Robert M Shelby, Conal Murray, Kenneth Rodbell, and Jeffrey Sleight. Performance stabilization of high-coherence superconducting qubits. *arXiv preprint arXiv:2503.12514*, 2025.
- <sup>42</sup>M Hegedüs, R Banerjee, A Hutcheson, T Barker, S Mahashabde, AV Danilov, SE Kubatkin, V Antonov, and SE de Graaf. In-situ scanning gate imaging of individual two-level material defects in live superconducting quantum circuits. *arXiv preprint arXiv:2408.16660*, 2024.
- <sup>43</sup>Alexander Bilmes, Alexander K Händel, Serhii Volosheniuk, Alexey V Ustinov, and Jürgen Lisenfeld. In-situ bandaged josephson junctions for superconducting quantum processors. *Superconductor Science and*

- Technology*, 34(12):125011, October 2021.
- <sup>44</sup>Etienne Daum, Benedikt Berlitz, Steffen Deck, Alexey V Ustinov, and Jürgen Lisenfeld. Investigation of parasitic two-level systems in merged-element transmon qubits. *arXiv preprint arXiv:2509.22593*, 2025.
- <sup>45</sup>Alexander Bilmes, Serhii Volosheniuk, Jan David Brehm, Alexey V Ustinov, and Jürgen Lisenfeld. Quantum sensors for microscopic tunneling systems. *npj Quantum Information*, 7(1):27, 2021.
- <sup>46</sup>Herve M Carruzzo, Alexander Bilmes, Jürgen Lisenfeld, Zheng Yu, Bu Wang, Zhongyi Wan, JR Schmidt, and Clare C Yu. Distribution of two-level system couplings to strain and electric fields in glasses at low temperatures. *Physical Review B*, 104(13):134203, 2021.
- <sup>47</sup>Yoni Shalibo, Ya'ara Rofe, David Shwa, Felix Zeides, Matthew Neeley, John M. Martinis, and Nadav Katz. Lifetime and coherence of two-level defects in a josephson junction. *Phys. Rev. Lett.*, 105:177001, Oct 2010.
- <sup>48</sup>Mo Chen, John Clai Owens, Harald Putterman, Max Schäfer, and Oskar Painter. Phonon engineering of atomic-scale defects in superconducting quantum circuits. *Science Advances*, 10(37):eado6240, 2024.
- <sup>49</sup>S Weeden, DC Harrison, S Patel, M Snyder, EJ Blackwell, G Spahn, S Abdullah, Y Takeda, BLT Plourde, JM Martinis, et al. Statistics of strongly coupled defects in superconducting qubits. *arXiv preprint arXiv:2506.00193*, 2025.
- <sup>50</sup>Hao Deng, Zhijun Song, Ran Gao, Tian Xia, Feng Bao, Xun Jiang, Hsiang-Sheng Ku, Zhisheng Li, Xizheng Ma, Jin Qin, et al. Titanium nitride film on sapphire substrate with low dielectric loss for superconducting qubits. *Physical Review Applied*, 19(2):024013, 2023.
- <sup>51</sup>Nikita S Smirnov, Elizaveta A Krivko, Anastasiya A Solovyova, Anton I Ivanov, and Ilya A Rodionov. Wiring surface loss of a superconducting transmon qubit. *Scientific Reports*, 14(1):7326, 2024.
- <sup>52</sup>John M Martinis. Surface loss calculations and design of a superconducting transmon qubit with tapered wiring. *npj Quantum Information*, 8(1):26, 2022.
- <sup>53</sup>Dmitry O Moskalev, Evgeniy V Zikiy, Anastasiya A Pishchimova, Daria A Ezenkova, Nikita S Smirnov, Anton I Ivanov, Nikita D Korshakov, and Ilya A Rodionov. Optimization of shadow evaporation and oxidation for reproducible quantum josephson junction circuits. *Scientific Reports*, 13(1):4174, 2023.
- <sup>54</sup>Daniel Thomas Sank. *Fast, accurate state measurement in superconducting qubits*. Phd thesis, University of California, Santa Barbara, 2014.

# Mapping the positions of Two-Level-Systems on the surface of a superconducting transmon qubit

Jürgen Lisenfeld, Alexander K. Händel, Etienne Daum, Benedikt Berlitz, Alexander Bilmes, and Alexey V. Ustinov

## SUPPLEMENTARY MATERIAL

### Supplementary Note A. SAMPLE FABRICATION AND PROPERTIES

The qubit sample investigated in this work was fabricated with the following recipe.

**Wafer preparation.** Sapphire wafers of 3 inch diameter and 500  $\mu\text{m}$  thickness are cleaned during 10 minutes in piranha solution and an additional exposure to  $O_2$ -plasma for 10 minutes before loading them into a Plassys eBeam-evaporator. During the following night, the Plassys is pumped and the wafer is tempered at 200°C for 2 hours.

The wafer is then coated by 100 nm of aluminum at a typical background pressure of  $1.4 \cdot 10^{-7}$  mBar. Before the coated wafer is exposed to atmosphere, it is oxidized for 10 minutes at 30 mBar  $O_2$  pressure.

**Dicing.** The 3-inch wafers are coated with a S1818 protective resist layer of  $\approx 1.8 \mu\text{m}$  thickness and diced into 2cm x 2cm large pieces. The diced wafers are cleaned in DMSO at 90°C without ultrasonic excitation to avoid damage of the aluminum layer by sapphire fragments from the dicing step.

**Optical lithography.** The cleaned 2x2 cm wafers are coated with a 170  $\mu\text{m}$ -thick layer of S1805 photoresist. The larger structures such as bonding pads, ground plane, resonators, qubit island, flux lines, and gate electrodes, are patterned via a photomask at a light intensity of 1.9 mW/cm<sup>2</sup> during 10 seconds and development in a 3:2 AZ-Developer and water mixture for about 30s. The aluminum layer is then dry-etched in an ArClO plasma (15 sccm Ar, 3sccm Cl, 1sccm O<sub>2</sub>) for 1 minute, and developed in DMSO at 90°C for 2-3 hours immediately after etching in order to prevent chlorine-induced corrosion.

**EBeam lithography.** The junctions are patterned by 3-angle shadow evaporation based on a Dolan-bridge process where unwanted stray junctions are shorted as explained in Ref. 43. To reduce aging effects, the wafer is afterwards oxidized in the evaporator's vacuum chamber in a clean Oxygen atmosphere of 30 mBar pressure. Final cleaning of the wafers occurs in DMSO at 90°C with ultrasonic excitation.

**Chip dicing.** The wafers are finally diced into chips of 6x6 mm size after additional coating with protective resist as described above.

Figure S1 shows a photograph of a finished chip. A summary of the qubit circuit parameters is given by Table S1.

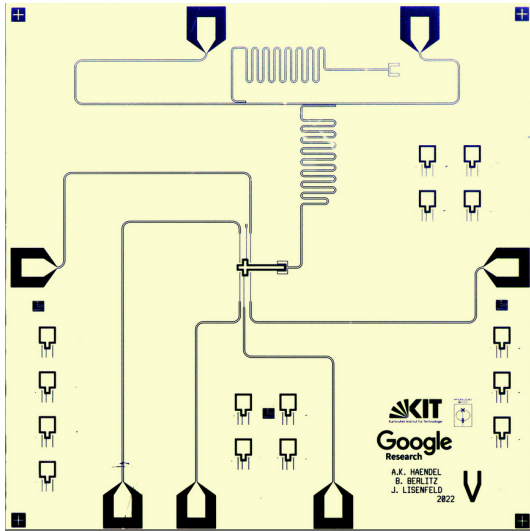


Fig. S1. Photograph of the qubit chip for TLS mapping.

name	value	description
$f_{\text{res,max}}$	7.83 GHz	resonator frequency at max. qubit frequency
$f_{\text{q,max}}$	5.56 GHz	maximum qubit frequency at zero flux
$T_{1,\text{max}}$	8 $\mu\text{s}$	observed maximum qubit $T_1$ time
$T_1$	5 $\mu\text{s}$	qubit $T_1$ -time averaged over frequency
$C_q$	84 fF	capacitance of qubit island to ground
$C_{q,\alpha}$	0.24 fF	capacitance of qubit island to $\alpha$ -electrode
$C_{q,\beta}$	0.29 fF	capacitance of qubit island to $\beta$ -electrode
$C_{q,\gamma}$	0.24 fF	capacitance of qubit island to $\gamma$ -electrode
$C_{q,\delta}$	0.29 fF	capacitance of qubit island to $\delta$ -electrode
$R_{n,\text{JJ}}$	14.5 k $\Omega$	room-temperature resistance of a single JJ
$R_{n,\text{SQ}}$	7.25 k $\Omega$	room-temperature resistance of a 2-JJ SQUID
$I_{c,\text{JJ}}$	23 nA	single-JJ critical current
$A_{\text{JJ}}$	0.08 $\mu\text{m}^2$	JJ area (for size $260 \pm 10 \text{ nm} \cdot 310 \pm 10 \text{ nm}$ )
$j_c$	285 nA/ $\mu\text{m}^2$	critical current density
$E_c/h$	229 MHz	qubit charging energy
$E_J/h$	23.4 GHz	qubit Josephson energy

Table S1. Measured and simulated fabrication parameters of the studied qubit sample. Capacitance values were extracted with Ansys Maxwell. Junction (JJ) and SQUID resistances are averages from 4-point measurements at room temperature.

### Supplementary Note B. EXPERIMENTAL SETUP

Figure S2 illustrates the experimental setup with the components for dispersive qubit readout, qubit flux biasing, and supply of voltage bias to the four on-chip gate electrodes.

The voltages for the on-chip gate electrodes are generated by a 16-bit DAC that is controlled via an optical connection to a PC, and then amplified to a range of  $\pm 250$  V using piezo drivers. The signals are transmitted via a copper wire loom to the qubit chip after passing through an LCR low-pass filter at the 4K-temperature stage. All measurements were done at a sample temperature of 25 - 30 mK.

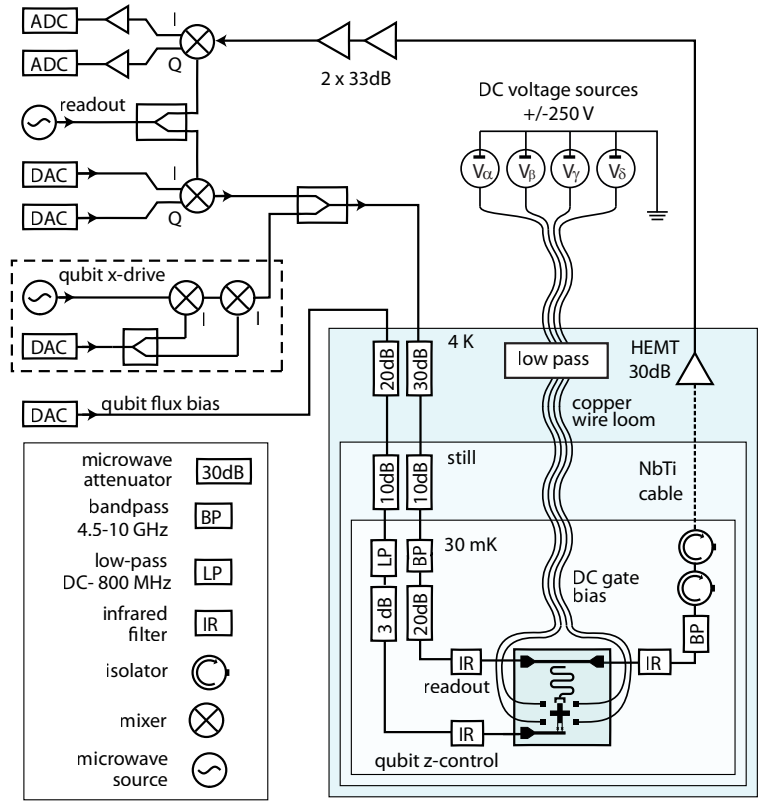


Fig. S2. Schematic of the experimental setup.

### Supplementary Note C. LOSS FROM GATE ELECTRODES

The qubit's energy relaxation rate is enhanced by its capacitive coupling to the gate electrodes. In order to increase the spatial resolution in TLS mapping, the electrodes have been placed in close vicinity to the qubit island as can be seen in the design shown in Figs. 1b and c. The resulting coupling capacitance between the qubit island and each gate electrode is  $C_{q,i} \approx 0.24 - 0.29$  fF as simulated with Ansys Maxwell, while the capacitance of the qubit island to ground is  $C_q = 84$  fF. This results in a loaded quality factor of the qubit given by<sup>39,54</sup>

$$Q_l = \left( \frac{C_{\text{tot}}}{C_c} \right)^2 \frac{Z_q}{\text{Re}(Z_{\text{eff}})}, \quad (\text{A1})$$

where  $C_{\text{tot}} = C_q + \sum_i C_{q,i}$  is the total capacitance, and  $Z_q = \sqrt{L_q/C_{\text{tot}}} \approx 290 \Omega$  is the qubit impedance estimated from the inductance of its two parallel Josephson junctions  $L_q = 0.5 \cdot L_J = 0.5 \cdot h/4\pi e I_c$  each having a critical current of  $I_c \approx 23$  nA as shown in Table Supplementary Note A. Assuming a real part impedance of  $\text{Re}(Z_{\text{eff}}) \approx 50 \Omega$  for the coplanar gate electrode including its feed line results in  $Q_l \approx 0.6$  million. The resulting loaded quality factor for all four electrodes is  $Q_{\text{tot}} = (4/Q_l)^{-1}$  and limits the qubit's energy relaxation time to  $T_1 = Q_{\text{tot}}/2\pi f_q \approx 5 \mu\text{s}$  at a qubit resonance frequency of  $f_q = 5$  GHz.

This estimated upper limit of  $T_1$  is in the range of the observed average qubit relaxation time  $T_1 \approx 8 \mu\text{s}$ . For comparison, equally fabricated qubit samples with comparable design

but without gate electrodes showed  $T_1$  times between 10 and 20  $\mu\text{s}$ . The actual impact of the gate electrodes on the  $T_1$  time remains unclear due to uncertainty about the gate electrode impedance, and the fact that only a single sample with on-chip gate electrodes was measured. To reduce this loss, the gate electrode impedance can be adjusted using on-chip shunt capacitors or inductors<sup>45</sup>.

### Supplementary Note D. ELECTRIC FIELD SIMULATIONS

For the TLS mapping procedure and the energy-participation-ratio (EPR) analysis, the AC-electric field distribution of the transmon qubit was simulated using ANSYS HFSS's Eigenmode Solver. The DC-electric fields emitted by the four gate electrodes were simulated with ANSYS MAXWELL, separately biasing each electrode with 1V. In all models, the simulation volume was restricted to a  $1\text{mm} \times 1\text{mm} \times 1\text{mm}$  large region centered around the qubit. All thin-film structures, including the qubit island, Josephson junctions, gate electrodes, resonator, bias line, and ground plane, were modeled as 2D sheets on a  $1\text{mm} \times 1\text{mm} \times 0.5\text{mm}$  sapphire substrate. Except for the junctions, all sheets were assigned the "Perfect E" boundary condition, while the junction sheets were assigned the "Lump RLC" boundary condition. Assuming a relative permittivity  $\epsilon_r = 10$  and thickness  $d = 2\text{nm}$  of the junction barrier, the applied junction capacitances  $C_{JJ}$  were estimated from the known junction area  $A$ , using  $C_{JJ} = A\epsilon_0\epsilon_r/d$ , to approximately 3.6 fF. The

junction inductances were adjusted such that the simulated eigenfrequency of the transmon qubit was approximately  $f_q \approx 5$  GHz. Along the edges of qubit sheets and the entire SQUID loop, the precision of the adaptive mesh solver was set to a minimum of 100 nm. Finally, the energy of the qubit mode was normalized to one photon to obtain the electric field strength  $E_{\text{rms}}$ .

Systematic offsets in the simulated electric field strength, e.g. due to averaging over simulation mesh elements, play a minor role since only relative field strengths are considered in the method. We used the same mesh for all simulations and increased the meshing resolution in a  $2 \mu\text{m}$  wide region around electrode edges. Systematic errors however do affect the estimation of the TLS dipole moments, which are directly calculated from the simulated local DC-field at the deduced TLS position and the measured TLS tuning strength. The steep gradient of  $E_{\text{rms}}$  near electrode edges enhances the uncertainty of the TLS dipole moment. Despite this, the obtained TLS dipole moments (Fig. 4b in the main manuscript) have a reasonable mean value and do not show excessive spread compared to other results<sup>37</sup>.

#### Supplementary Note E. TLS DETECTABILITY LIMITS

As described in the main text, TLS can only be detected in regions where the AC electric field of the qubit mode is above a minimum strength  $E_{\text{min}}$ . In this case, the TLS-qubit coupling energy exceeds  $g_{\text{min}} = p E_{\text{min}}$ , and when the qubit is in resonance with the TLS, the qubit  $T_1$  time is sufficiently suppressed so that the TLS is observed. Here,  $p$  is the component of the TLS' electric dipole moment that is parallel to the qubit's AC electric field, whose value can be estimated to  $p_{\parallel} \approx 1 e\text{\AA}$  in accordance to measurements<sup>3,4,6,33,37,47,48</sup> and atomistic simulations<sup>15,16</sup>.

When a moderately coupled TLS is near resonance with the qubit, it causes a Lorentzian peak in the qubit's energy relaxation rate  $\Gamma_1 \equiv 1/T_1$ , which in the limit of  $\Gamma_{1,\text{TLS}} > g/h > \Gamma_{1,q}$  is described (see supplementary material to<sup>26</sup>)

$$\Gamma_1 = \frac{2(g/h)^2 \Gamma}{(\Gamma/2\pi)^2 + \delta^2} + \Gamma_{1,q}. \quad (\text{A2})$$

Here,  $\Gamma = \Gamma_{1,\text{TLS}}/2 + \Gamma_{2,\text{TLS}} + \Gamma_{1,q}/2 + \Gamma_{2,q}$  is the sum of TLS and qubit energy relaxation and dephasing rates, and  $\delta$  is the detuning between qubit and TLS.

Solving for the coupling strength  $g$  where Eq. (A2) predicts that the qubit's energy relaxation time at resonance  $\delta = 0$  is decreased by a factor  $\kappa$  then results in the minimum coupling strength  $g_{\text{min}} = \hbar \sqrt{\kappa \cdot \Gamma_{1,q} \Gamma / 2}$  and corresponding minimum AC-electric qubit field strength  $E_{\text{min}} = g_{\text{min}} / p_{\parallel}$ .

Figure S3 shows  $E_{\text{min}}$  vs. the detection factor  $\kappa$  for different TLS dipole moment sizes  $p_{\parallel}$  and a qubit  $T_1$  time of  $7 \mu\text{s}$  as in our experiment.

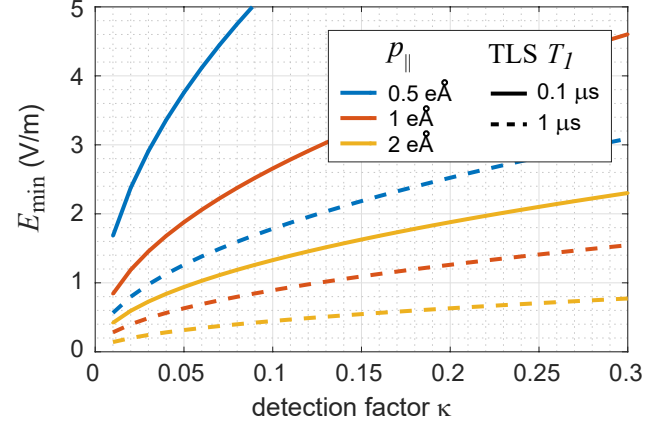


Fig. S3. Minimum qubit AC-electric field strength  $E_{\text{min}}$  at the TLS position for which the qubit  $T_1$ -time is reduced by more than the detection factor  $\kappa$  at resonance. For this plot, the isolated qubit  $T_1$  time is set to  $7 \mu\text{s}$ . The colors correspond to different TLS electric dipole moments. Solid and dashed lines are plotted for TLS  $T_1$  times of  $0.1 \mu\text{s}$  and  $1 \mu\text{s}$ , respectively.

The minimum field  $E_{\text{min}}$  decreases for more coherent TLS. In experiments, TLS energy relaxation times of  $T_{1,\text{TLS}} \approx 0.1 - 0.2 \mu\text{s}$  are most commonly observed<sup>4,6,33,43,47,48</sup>. However, also TLS are observed which have longer coherence times in a range of a few  $10 \mu\text{s}$ . These may be better decoupled from the phonon bath<sup>48</sup>, for example due to a symmetry of the tunneling wavefunction, or because of a reduced local phonon spectrum e.g. at material interfaces.

The region of a qubit circuit within which TLS can be detected is bounded by  $E_{\text{min}}$  and increases with the qubit coherence time  $T_1$  as shown in Fig. S4. More coherent qubits are thus affected by a larger number of TLS, including those residing farther away from the electrode edges.

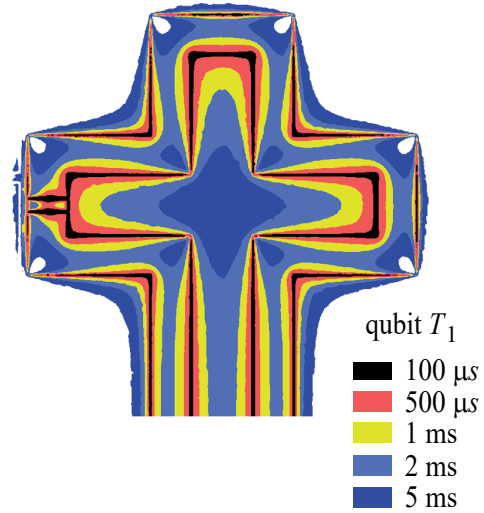


Fig. S4. The region where TLS interact sufficiently strongly to be detected in TLS spectroscopy depends on the  $T_1$  time of the qubit, as indicated by the different colors. The plot was made with an Ansys HFSS simulation of the qubit's AC electric field strength, assuming a TLS coherence time of  $100\text{ns}$ , a TLS dipole moment of  $1 e\text{\AA}$ , and a detection factor of  $\kappa = 0.1$ .

**Energy participation ratio (EPR).** The probability to detect a TLS increases with the square of the local qubit

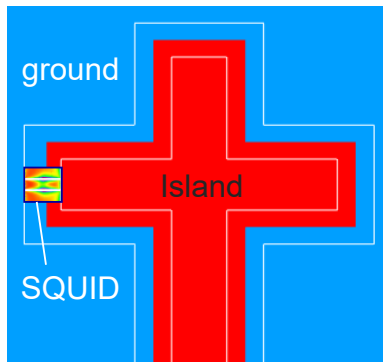


Fig. S5. Areas assigned to the ground plane (blue), the qubit island (red), and the SQUID (indicated square), as used for calculating energy participation ratios. The white lines indicate electrode edges.

AC-field, since the qubit decay rate  $\Gamma_1$ , which is used as the signal in swap spectroscopy, scales with the qubit-TLS coupling strength  $g^2 \propto |E_{\text{rms}}|^2$  (see Eq. A2 and definition of  $g$  in the main text). This is analogous to surface loss analyses which consider the energy participation ratio (EPR) of different circuit areas, i.e. the fraction of the qubit energy that is stored there<sup>14</sup>. We thus estimate the expected ratio of the numbers of TLS observed on the SQUID vs. those on the qubit capacitor by comparing integrals over  $|E_{\text{rms}}|^2$  in the vicinity of these elements.

For this, the simulated  $|E_{\text{rms}}|$  is exported on a rectangular grid, and the sum of  $|E_{\text{rms}}|^2$  is calculated for pixels inside the SQUID and capacitor areas whose dimensions are shown in Fig. S5. Moreover, this sum is limited to regions where  $|E_{\text{rms}}| > E_{\text{min}}$ , in order to account for the detectability of TLS in swap spectroscopy. The resulting EPRs of SQUID and ground+island are shown in the main text's Fig. 4c as a function of the chosen value of  $E_{\text{min}}$ .

**Field directions.** The method to find TLS positions requires that the gate electrode fields are parallel at the position of the TLS. This is confirmed with Fig. S7 also for the region near the Josephson junctions. Fig. S7a shows the strength of the qubit's AC-electric field  $|E_{\text{rms}}|$  and a zoom onto the DC-SQUID. A vertical cross-section is shown in Fig. S7b, where the junction leads are indicated by gray bars that are separated by  $6 \mu\text{m}$ . The region where  $|E_{\text{rms}}| > E_{\text{min}}$  (here for  $E_{\text{min}}=0.75 \text{ V/m}$ ) is shaded red. Directly at the junctions, the detection region extends up to  $1.8 \mu\text{m}$  distance from the lead edges. Similar to Fig. 3 in the main text, the  $\vec{x}$ - and  $\vec{z}$ -directions of the electric fields are plotted in Fig. S7c, and their vector products shown in Fig. S7d indicate that they are practically parallel within the vicinity of junction leads.

#### Supplementary Note F. DATA ACQUISITION AND TLS PROPERTIES

In the TLS swap-spectroscopy measurements as shown in Fig. 2a, the qubit was swept in a frequency range from 5.05 GHz to 5.20 GHz in steps of 0.375 MHz. In each segment,

the voltage of a different gate electrode was increased by 1V in steps of 50 mV. The total voltage on each electrode was swept from -60 V to +100 V to acquire a total number of 640 segments.

We have identified the resonant traces of 55 individual TLS whose response to all four gate electrodes was observed in the investigated frequency range, allowing those to be further analyzed. Each segmented hyperbolic trace was manually marked and fit to Eq. 1 to obtain the TLS' response factors  $\gamma_i$ , which are plotted in Fig. S5. We acquired data during 33 days, comprising over 5 million individual (averaged) measurements at a rate of 2 measurements / second. The measurement duration could be reduced to about 1 day by using faster electronics, a Josephson parametric amplifier, and active qubit reset techniques.

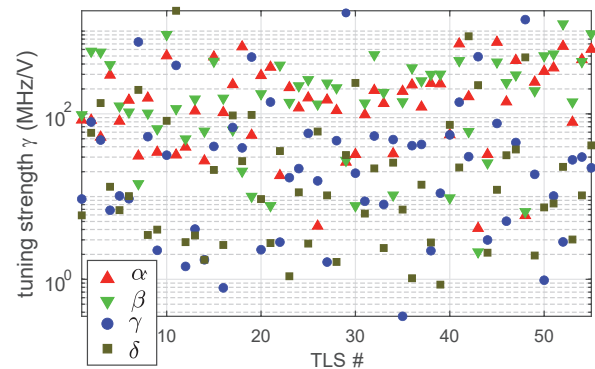


Fig. S6. Tuning strengths  $\gamma_i$  for the four gate electrodes  $i \in \{\alpha, \beta, \gamma, \delta\}$ , obtained for 55 TLS by fitting their swap-spectroscopy traces to Eq. (1).

#### Supplementary Note G. RESOLUTION IN TLS MAPPING

The precision in the determination of TLS positions depends mostly on the uncertainties in the tuning strengths  $\gamma_i$  measured in segmented swap spectroscopy as shown in Fig. 2a. If a TLS is located at a larger distance from an electrode, its weaker response results in a less precise fit estimate. This can be mitigated by a more appropriate qubit and gate electrode design that aims to enhance the overlap of the electric fields.

Moreover, TLS which respond strongly to one electrode may be quickly tuned through most of the observed swap spectroscopy range, reducing the available data on the response to more distant electrodes. This problem can be avoided with a measurement protocol where the gate voltages are reset to an initial value after they were swept. This would also allow one to increase the swept voltage range to facilitate measurements of weak responses to some electrodes.

As an example of the resolution limit, Fig. S8 shows data of a TLS that is determined to reside near the qubit's Josephson junctions. There is some uncertainty whether the TLS resides on the upper or lower branch of the DC-SQUID. While most observed tuning ratios indicate a position on the upper branch, the data for  $\gamma_\alpha/\gamma_\gamma$  (lower left panel in Fig. S8) suggests a solution on the lower branch. This may be due to the fit error determining the relatively weak  $\gamma$ -gate response  $\gamma_\gamma$ . The SQUID branches are separated by a distance of  $6 \mu\text{m}$  (see also Fig. 1d). We expect that in our experiment, the achieved resolution is of similar size, and believe that it could be reduced to a few micrometers by mentioned improvements in

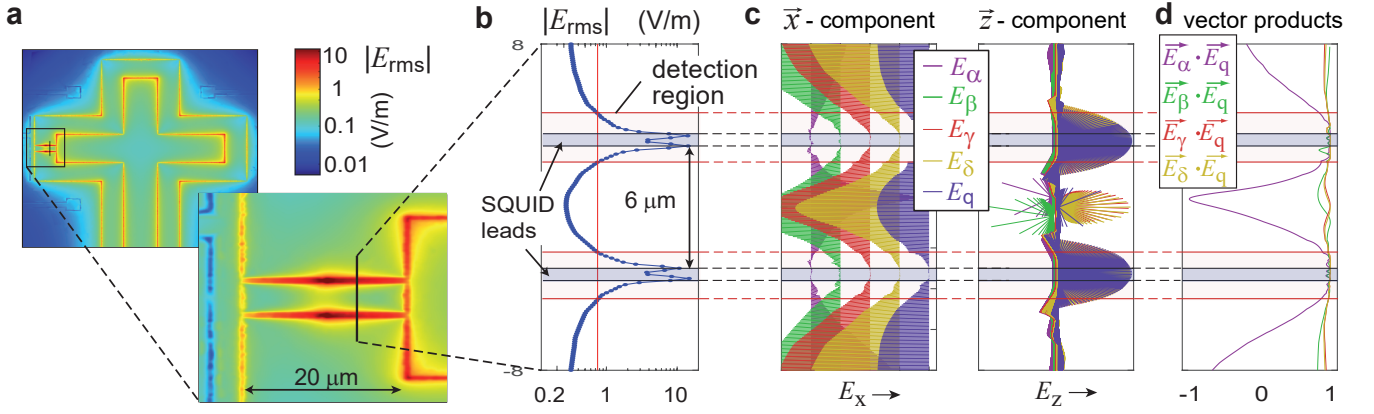


Fig. S7. **Strength and orientations of AC- and DC-electric fields near the DC-SQUID.** **a** Magnitude of the qubit's AC-electric field  $|E_{\text{rms}}|$  as simulated with Ansys HFSS, with a zoom onto the DC-SQUID. **b** Cross-section of  $|E_{\text{rms}}|$  along the black line in **a**. TLS can be detected in the red-shaded area where the field exceeds a minimum strength  $E_{\text{min}}$ . **c** Components of the electric fields from the four electrodes and the qubit, plotted in  $\vec{x}$ - and  $\vec{z}$  directions (left and right panel). **d** The normalized vector product between the fields of gate electrodes and the qubit indicates that they are practically parallel in the range where TLS can be detected.

sample design and measurement protocol.

We tested the impact of errors on the measured TLS-electrode coupling strengths  $\gamma_i$  with Monte-Carlo-simulations. For this, a TLS position was manually selected, and the exact tuning ratios at this position were determined from the E-field simulation. To simulate measurement uncertainty, these exact ratios were multiplied by random factors that have a constant distribution in an interval of  $1 \pm \delta$ , where the maximum variation  $\delta$  ranges from 1% to 50%. From these noisy tuning ratios, the TLS position was then determined with the mapping algorithm.

For a TLS placed on the SQUID and for a TLS on the qubit island, Fig. S9 and Fig.S10 respectively show resulting TLS positions from 1000 iterations (panels **a** and **d**). The deviations from the exact TLS location are shown in panels **b** for different variation factors  $\delta$ , and in panel **e** for differently chosen cut-off of the minimum electric field  $E_{\text{min}}$  that limits the detection area. We find that the median deviation between estimated and exact TLS positions ranges between  $2 \mu\text{m}$

and  $8 \mu\text{m}$  for variation factors up to  $\delta = 50\%$ , while for factors of  $\delta > 20\%$ , the TLS position on the SQUID can not anymore reliably distinguished from a position on the island or ground plane. When the detection area is not restricted at small values of  $E_{\text{min}}$ , TLS are mostly placed further away from the electrodes (see Fig. S9d). Such solutions are invalid since at these positions, TLS would not be observed in our TLS spectroscopy, and because the electric fields from the four electrode are not necessarily parallel, e.g. in the gap between ground plane and qubit island.

Before analyzing the data, we excluded several detected traces of TLS whose coupling strengths to the upper electrodes ( $\alpha$  and  $\gamma$  in Fig. 1) were indistinguishable from zero so that their position can not be reliably determined with the current procedure. These traces stem from TLS that are located further away on the extended arm of the qubit island (see Fig. 1b). Accordingly, possible solutions for TLS positions were restricted to the  $105 \mu\text{m} \times 105 \mu\text{m}$ -large window as shown in Fig. 1c.

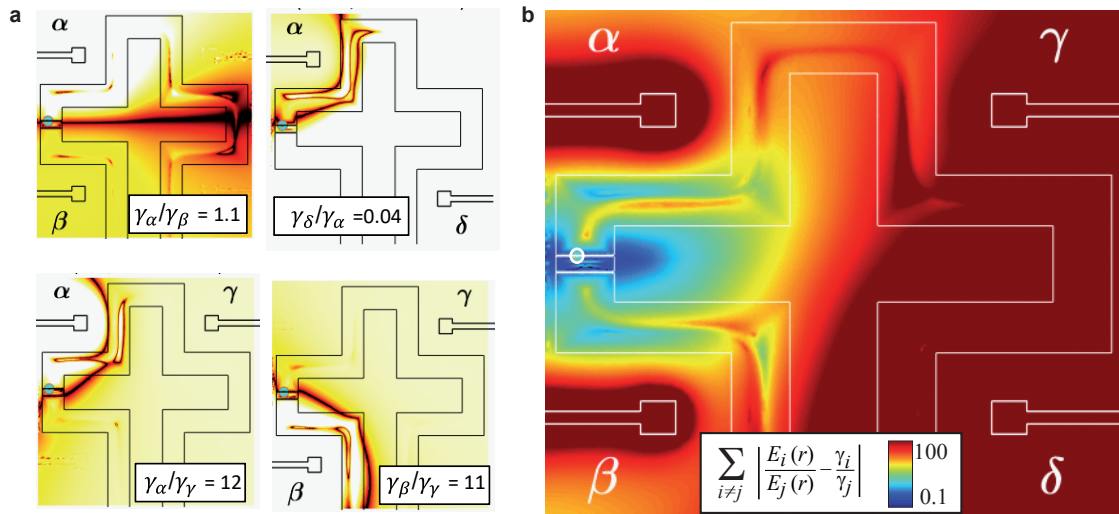


Fig. S8. Data of a TLS that is identified to reside on the qubit's DC-SQUID, similar to Figs. 2b,c. **a b** Difference sum  $\sigma$  (Eq. 3) over all 6 unique combinations of electrode pairs. The white circle marks the global minimum, placing the TLS on the upper branch of the DC-SQUID's loop.

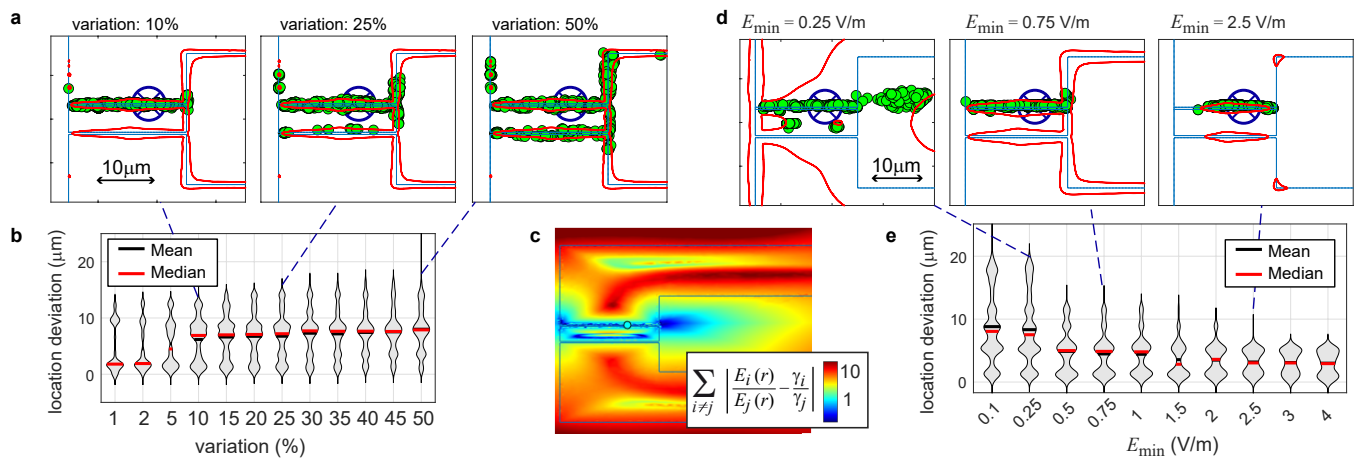


Fig. S9. **a** Determined positions (green circles) of a TLS on the DC-SQUID, whose exact location is marked by the blue circle, for different levels of noise (variation factor  $\delta$ ) in the determined tuning ratios. **b** Histograms of deviations from the exact TLS position for different levels of variation  $\delta$ . **c** Difference between simulated E-field strengths and TLS tunability as in Fig. 2c, where minima (blue pixels) indicate most likely TLS positions. **d** Same as **a**, but varying the value of  $E_{\min}$  that limits the detection area. **e** Deviations from the exact TLS location vs.  $E_{\min}$ . For Figs. **a, b**,  $E_{\min} = 1$  V/m, and for Figs. **d, e**, the variation was fixed at  $\delta = 10\%$

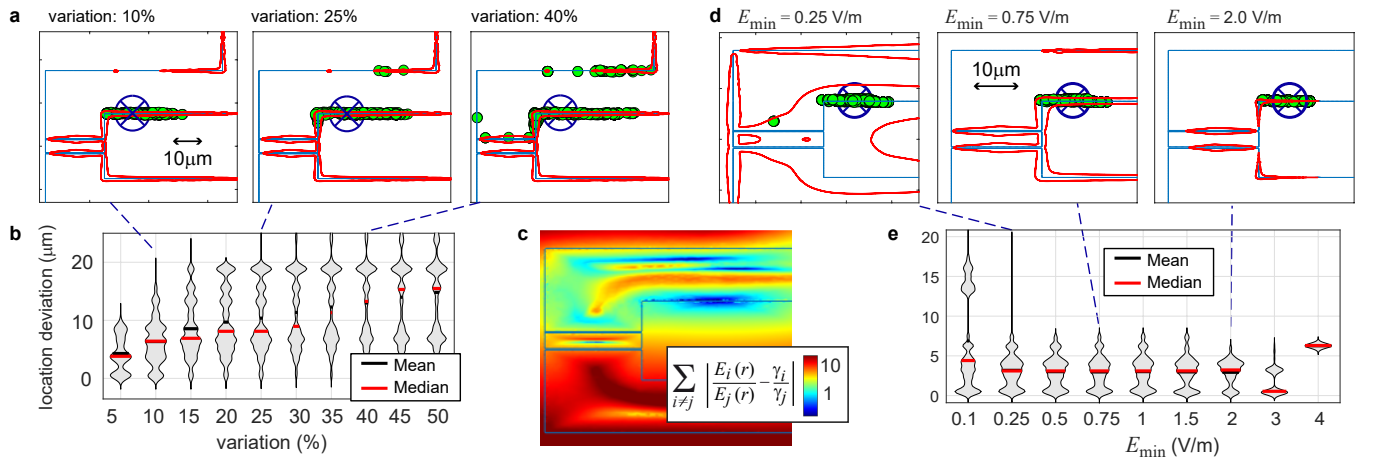


Fig. S10. Determined positions (green circles) of a TLS on the qubit island (blue circle), similar to Fig. S9. **a** and **d** Positions for different variation factors  $\delta$  and values of  $E_{\min}$ , respectively, **b** and **e**: Histograms of deviations from the exact TLS position for different levels of variation  $\delta$ , and for different values of  $E_{\min}$ , respectively. **c** Difference between simulated E-field strengths and TLS tunability.